Engineering Transactions, **74**(2): 145–171, 2026, https://doi.org/10.24423/engtrans.2025.3639
Institute of Fundamental Technological Research Polish Academy of Sciences (IPPT PAN)
Université de Lorraine • Poznan University of Technology

Research Paper

Numerical Modeling of the Aluminum Alloy AW5083 Using Large-Strain Thermo-Elasto-Plasticity

Agnieszka Sobierańska, Balbina Wcisło*

Chair of Computational Engineering, Cracow University of Technology
Kraków, Poland

*Corresponding Author: balbina.wcislo@pk.edu.pl

This paper deals with the constitutive modeling and finite element (FE) simulations of advanced models related to large-strain thermo-elasto-plastic behavior of aluminum alloy AW5083, which can reproduce the material response at different temperatures from room temperature up to 500 °C. Significant focus is placed on internal sources of cooling and heating resulting from thermo-elastic and thermo-plastic couplings, respectively, and on the influence of elevated temperature on these couplings. The formulation of the constitutive description is based on a thermodynamic approach. Two models are presented and tested, including temperature-dependent and temperature-independent plastic free energy function. Numerical tests of the developed models are carried out for a uniaxial tensile test. For the sake of comparison with experimental results, a dogbone specimen examined in a tensile machine is analyzed.

Keywords: aluminum alloy AW5083, thermo-elasto-plasticity, temperature dependent parameters, large-strains, finite element method.

1. Introduction

This paper presents a constitutive modeling and a numerical investigation of aluminum alloy AW5083 using a large-strain thermo-elasto-plastic model that incorporates internal heat sources and temperature-dependent material parameters.

Various large strain thermo-elasto-plasticity models can be found in the literature. This work is focused on thermodynamically consistent models presented, e.g., in [1, 2], derived based on the first and second laws of thermodynamics. Such an approach leads to a formulation that involves internal (often called structural) sources of cooling or heating in the analyzed material. In particular, thermo-elastic coupling related to the Gough–Joule effect, typically associated

with entropic materials such as polymers [3], manifests itself in aluminum as cooling in tensioned samples in the elastic regime, whereas the thermomechanical coupling in plasticity results in temperature increase due to plastic dissipation. The crucial quantity in these formulations is the Helmholtz free energy, which can include a reversible part (related to elasticity and thermal expansion), a plastic part, and a purely thermal part [2].

Constitutive modeling of an aluminum alloy undergoing large strains at elevated temperatures requires the introduction of temperature-dependent material parameters. Such models are included in some papers, e.g., in [4], presenting a small-strain constitutive model for case-hardening steel, or in [5] related to thermo-elasto-plasticity of metals with material properties being linear functions of temperature. In this work, the material model based on [2] is enhanced with dependencies of material properties on temperature, based on [6, 7]. Moreover, the study focuses on two distinct models of the plastic part of the free energy: one that accounts for temperature-dependent material parameters in the free energy formulation and another that assumes temperature-independent hardening in plasticity.

The goal of this research is to develop and test a comprehensive constitutive framework capable of accurately predicting the response of aluminum alloy AW5083 under mechanical loads at different temperatures, ranging from 20 °C up to 500 °C. The research is a continuation of the work presented in [8], which was restricted to room temperature. The following assumptions are taken into account in the research. The material is initially isotropic, also regarding hardening in plasticity, and associative plastic flow is applied. The model reproduces the quasi-static case; thus, it does not include viscous effects in elasticity or in plasticity and the inertial term in the balance of linear momentum is dropped. The thermomechanical coupling incorporates thermal expansion, temperature-dependent parameters, internal heat sources and the influence of geometry change on the heat flow in the material, i.e., it takes into account Fourier's law in the deformed configuration.

This advanced and strongly non-linear model is implemented and tested utilizing symbolic-numerical packages AceGen/AceFEM of Wolfram Mathematica [9]. Simulations are performed for a uniaxial tension test and for a dogbone specimen typically used in experimental conditions [10]. By comparing the selected models, the paper aims to show the influence of temperature-hardening coupling on the mechanical and thermal behavior of the material. The key phenomena of thermo-elastic cooling and heat generation due to plastic dissipation are analyzed in detail. Through numerical simulations of the dogbone specimen, the study explores the effects of temperature-dependent parameters, mesh refinement sensitivity, and thermal boundary conditions on the specimen's response. The results highlight the significance of thermo-plastic coupling in the

plastic part of the free energy in reducing self-heating and softening effects, particularly in the temperature range from 200 °C to 300 °C. The paper also addresses different forms of localization.

The research presented in the paper can be applied to advanced numerical simulations of structures and elements made of aluminum alloy AW5083, which is widely used in shipbuilding, railroad cars, pressure vessels, and many other fields, under various mechanical and/or thermal loading. The development of a formulation valid at elevated temperatures enables simulations under fire conditions.

The paper is laid out as follows. Section 2 presents the formulation of the thermo-elasto-plastic material model based on the laws of thermodynamics. Section 3 contains functional dependencies of material parameters, both the mechanical and thermal ones, with respect to temperature. The core part of the paper is Sec. 4 including the description and results of numerical simulations, whereas conclusion and final remarks are provided in Sec. 5.

The notation used in the paper is as follows: round brackets introduce arguments of functions, whereas square brackets specify the sequence of operations.

2. Model of material

2.1. Kinematics

The material description developed in the paper is based on a thermo-elasto-plastic model presented in [2]. The model is based on the decomposition of the deformation gradient into a reversible part $\mathbf{F}^r$, related to elastic deformation and thermal expansion, and an irreversible (plastic) part $\mathbf{F}^p$ in the following form:

$$\mathbf{F} = \mathbf{F}^r\mathbf{F}^p. \tag{2.1}$$

The deformation gradient is defined in the standard form as $\mathbf{F} = \partial\mathbf{x}(\mathbf{X}, t)/\partial\mathbf{X}$ with $J = \det(\mathbf{F}) > 0$, where $\mathbf{X}$ and $\mathbf{x}$ are vectors denoting the referential and the current placement of a particle in the Cartesian coordinate system, respectively, and the variable t represents time. Based on the decomposition (2.1), the reversible left Cauchy–Green tensor is defined as follows:

$$\mathbf{b}^r = \mathbf{F}^r(\mathbf{F}^r)^{\mathrm{T}}, \qquad J^{br} = \det(\mathbf{b}^r). \tag{2.2}$$

The velocity gradient and its symmetric part, called the deformation rate, are defined as usual:

$$\mathbf{l} = \dot{\mathbf{F}}\mathbf{F}^{-1}, \qquad \mathbf{d} = \frac{1}{2}\left(\mathbf{l} + \mathbf{l}^{\mathrm{T}}\right), \tag{2.3}$$

where the dot over a quantity denotes its rate. The plastic velocity gradient is defined as follows:

$$\mathbf{L}^p = \dot{\mathbf{F}}^p \left[\mathbf{F}^p\right]^{-1}, \tag{2.4}$$

and the plastic deformation rate:

$$\mathbf{d}^p = \frac{1}{2}\left(\mathbf{l}^p + \left[\mathbf{l}^p\right]^{\mathrm{T}}\right), \qquad \mathbf{l}^p = \mathbf{F}^r \mathbf{L}^p \left[\mathbf{F}^{\mathbf{r}}\right]^{-1}. \tag{2.5}$$

The Helmholtz free energy is assumed to depend on the reversible left Cauchy–Green deformation tensor $\mathbf{b}^r$, the internal variable α related to hardening, and the absolute temperature T:

$$\psi = \psi(\mathbf{b}^r, \alpha, T). \tag{2.6}$$

The specific form of the Helmholtz free energy will be given in the subsequent subsection.

2.2. Governing equations

The first governing equation, i.e., the balance of linear momentum for the large-strain problem, is written for the quasi-static case with mass forces neglected [11]:

$$\operatorname{div}\left(\boldsymbol{\tau}/J\right) = \mathbf{0}, \tag{2.7}$$

where the symbol $\operatorname{div}(\cdot)$ denotes the spatial divergence of the quantity $\cdot$, and $\boldsymbol{\tau}$ is the Kirchhoff stress tensor. The quasi-static assumption results in neglecting the inertial term in Eq. (2.7). The model can then be applied to simulate deformation at low-strain rates. Consequently, viscous effects are also neglected.

The second governing equation is the first law of thermodynamics, i.e., the balance of energy, which can be written using spatial quantities [2]:

$$\rho \dot{u} = \boldsymbol{\tau} : \mathbf{d} - J \operatorname{div}(\mathbf{q}), \tag{2.8}$$

where ρ is the material density of the undeformed configuration which can be temperature-dependent, u is the internal energy per unit of mass, and $\mathbf{q}$ is the Kirchhoff heat flux density vector. In Eq. (2.8), an external heat source (per unit of mass) is not taken into account.

The second law of thermodynamics, i.e., the dissipation inequality, can be written in the following form [2]:

$$\rho T \dot{\eta} - \rho \dot{u} + \boldsymbol{\tau} : \mathbf{d} - \frac{J}{T} \mathbf{q} \cdot \operatorname{grad}(T) \geq 0, \tag{2.9}$$

where η denotes the entropy per unit of mass and grad $(\cdot)$ is the spatial gradient of quantity $\cdot$. Using the Legendre transformation:

$$\psi(\mathbf{b}^r, \alpha, T) = u(\mathbf{b}^r, \alpha, \eta - \eta T), \tag{2.10}$$

after some manipulations, the dissipation inequality can be written as

$$\left[\boldsymbol{\tau} - 2\rho\frac{\partial\psi}{\partial\mathbf{b}^r}\right] : \mathbf{d} + \left[2\rho\frac{\partial\psi}{\partial\mathbf{b}^r}\mathbf{b}^r\right] : \mathbf{d}^p - \rho\frac{\partial\psi}{\partial\alpha}\dot{\alpha} - \frac{J}{T}\mathbf{q}\cdot\operatorname{grad}(T) \geq 0. \tag{2.11}$$

Because inequality (2.11) should be fulfilled for any arbitrary $\mathbf{d}$, the Kirchhoff stress tensor is equal to:

$$\boldsymbol{\tau} = -2\rho\frac{\partial\psi}{\partial\mathbf{b}^r}. \tag{2.12}$$

The thermodynamic force conjugated to α is defined as

$$\beta = \rho\frac{\partial\psi}{\partial\alpha}. \tag{2.13}$$

Now, the reduced form of the dissipation inequality is obtained:

$$\underbrace{[\boldsymbol{\tau} : \mathbf{d}^p - \beta\dot{\alpha}]}_{\mathcal{D}_{\text{mech}}} + \underbrace{\left[-\frac{J}{T}\mathbf{q}\cdot\operatorname{grad}(T)\right]}_{\mathcal{D}_{\text{therm}}} \geq 0. \tag{2.14}$$

It is assumed that both parts of the dissipation, mechanical $\mathcal{D}_{\text{mech}}$ and thermal $\mathcal{D}_{\text{therm}}$, are greater than or equal to 0. In the latter case, the inequality is fulfilled by the application of the isotropic spatial Fourier law as the constitutive relationships for the heat flux density vector, for details see [12],

$$\mathbf{q} = -Jk\operatorname{grad}(T), \tag{2.15}$$

where k is the conductivity coefficient, which can be temperature-dependent, i.e., $k(T)$.

Using Eq. (2.10) and Eq. (2.11), the energy balance Eq. (2.8) can be rewritten in the so-called temperature form, which will be further implemented in numerical simulations:

$$c\dot{T} = J\operatorname{div}(\mathbf{q}) + \mathcal{D}_{\text{mech}} + \mathcal{H} + \mathcal{A}, \tag{2.16}$$

where

$$c = -\rho T\frac{\partial^2\psi}{\partial T^2}, \tag{2.17}$$

$$\mathcal{H} = \left[2\rho T \frac{\partial^2 \psi}{\partial T \partial \mathbf{b}^r} \mathbf{b}^r\right] : [\mathbf{d} - \mathbf{d}^p], \tag{2.18}$$

$$\mathcal{A} = \rho T \frac{\partial^2 \psi}{\partial T \partial \alpha} \dot{\alpha}. \tag{2.19}$$

In Eq. (2.16), there are three internal (structural) sources of heating/cooling, which can change the temperature of the material even if there are no external heat sources. $\mathcal{D}_{\text{mech}}$ is related to the heat production during a plastic process and $\mathcal{H}$ to the thermo-elastic source of heating/cooling. The term $\mathcal{A}$ is in turn a source related to the coupling between hardening in plasticity and temperature, which will further be called temperature-hardening coupling. This term is active when the plastic part of the free energy function is temperature-dependent.

Note that the internal sources depend on the adopted form of the Helmholtz free energy which will be specified in the next subsection.

2.3. Helmholtz free energy

In this paper, the following decoupled form of the Helmholtz free energy is adopted:

$$\psi = \psi^r(\mathbf{b}^r, T) + \psi^p(\alpha, T) + \psi^\theta(T), \tag{2.20}$$

where ψ^r is the free energy related to the reversible deformation due to elastic response and thermal expansion, ψ^p is the plastic part, which can be dependent on the hardening variable and optionally on temperature. The reversible part of the free energy follows the neo-Hookean formulation, which is a basic approach for elastic materials in a large deformation framework. The last term ψ^θ is the purely thermal part. The specific form of reversible Helmholtz free energy is as follows:

$$\psi^r(\mathbf{b}^r, T) = \frac{1}{\rho(T)} \left[\frac{\kappa(T)}{2} \left[\ln\left(\sqrt{J^{br}}\right)\right]^2 + \frac{G(T)}{2} \left[\operatorname{tr}\left([J^{br}]^{-1/3}\, \mathbf{b}^r\right) - 3\right] - 3\kappa\, \alpha_T(T)\, [T - T_0] \ln\left(\sqrt{J^{br}}\right)\right]. \tag{2.21}$$

The temperature-dependence of the material parameters present in Eq. (2.21) is now explicitly written. The symbol κ denotes the bulk modulus, G – the shear modulus, and α_T – thermal expansion coefficient.

The plastic part of the free energy is related to exponential hardening which is observed for the considered aluminum alloy, cf. [6, 10]. The form of the plastic

part of the free energy influences also the source defined in Eq. (2.19). In this study, two models are compared.

The first one, hereafter called Model 1, incorporates the plastic free energy function depending on the hardening variable and temperature. The temperature dependency is achieved by the application of temperature-dependent parameters: the initial and final yield stresses σ_{y0} and $\sigma_{y\infty}$, respectively, as follows:

$$\psi^p(\alpha, T) = \frac{1}{\rho(T)} \left[\sigma_{y\infty}(T) - \sigma_{y0}(T)\right] \left[\alpha + \frac{1}{\delta} \exp(-\delta\alpha)\right]. \tag{2.22}$$

The final yield stress represents the saturated flow stress, i.e., the maximum stress level the material can reach after a large amount of plastic deformation, when further hardening becomes negligible. Examples of such assumption can be found, e.g., in [5]. For Model 1, the temperature-hardening coupling is present and in the energy balance Eq. (2.16) the term $\mathcal{A}$ in non-zero. The saturation parameter δ in Eq. (2.22) is assumed in the paper as constant.

The second model, called hereafter Model 2, includes a temperature-independent plastic part of the free energy function:

$$\psi^p(\alpha) = \frac{1}{\rho(T)} \left[\sigma_{y\infty}(T_0) - \sigma_{y0}(T_0)\right] \left[\alpha + \frac{1}{\delta} \exp(-\delta\alpha)\right], \tag{2.23}$$

and involves the values of the initial and final yield stresses at initial temperature of the experiment T_0. The temperature-independent plastic part of the free energy function is used, e.g., in [4].

The thermal part of the free energy is not specified here explicitly. It is assumed that it has a form such that the heat capacity from Eq. (2.17) is temperature-dependent in a form given, in the next section.

2.4. Plasticity

The yield function is assumed in the following form:

$$\mathcal{F} = f(\boldsymbol{\tau}) - \sigma_y(\alpha, T) \leq 0, \tag{2.24}$$

where $f(\boldsymbol{\tau})$ is a stress measure governing plasticity. Here, the Huber–Mises measure is applied:

$$f(\boldsymbol{\tau}) = \sqrt{\mathbf{t} : \mathbf{t}}, \qquad \mathbf{t} = \boldsymbol{\tau} - \frac{1}{3}\mathrm{tr}\,(\boldsymbol{\tau})\,\mathbf{I}. \tag{2.25}$$

The yield stress $\sigma_y(\alpha, T)$ for Model 1 is as follows:

$$\begin{aligned} \sigma_y(\alpha, T) &= \sigma_{y0}(T) + \beta(\alpha, T) \\ &= \sigma_{y0}(T) + \left[\sigma_{y\infty}(T) - \sigma_{y0}(T)\right] \left[1 - \exp(-\delta\alpha)\right], \end{aligned} \tag{2.26}$$

whereas for Model 2 it is as follows:

$$\sigma_y(\alpha,T) = \sigma_{y0}(T) + s(T)\beta(\alpha) = \sigma_{y0}(T) + s(T)\left[\sigma_{y\infty}(T_0) - \sigma_{y0}(T_0)\right]\left[1-\exp(-\delta\alpha)\right], \tag{2.27}$$

where the thermal softening function $s(T)$ is proposed in the following form to obtain the same yield stress as in Model 1:

$$s(T) = \frac{\sigma_{y\infty}(T) - \sigma_{y0}(T)}{\sigma_{y\infty}(T_0) - \sigma_{y0}(T_0)}. \tag{2.28}$$

The associative flow rule is adopted in the following form:

$$-\frac{1}{2}\mathcal{L}_v(\mathbf{b}^r) = \dot{\gamma}\frac{\partial \mathcal{F}}{\partial \boldsymbol{\tau}}\mathbf{b}^r, \tag{2.29}$$

where the Lie derivative of the reversible left Cauchy–Green deformation tensor is defined as [2]:

$$\mathcal{L}_v(\mathbf{b}^r) = \mathbf{F}\frac{\partial}{\partial t}\left[\mathbf{F}^{-1}\mathbf{b}^r\mathbf{F}^{-T}\right]\mathbf{F}^{\mathrm{T}}, \tag{2.30}$$

where $\dot{\gamma}$ is the plastic multiplier, which is related to the hardening variable through the equation $\alpha = \sqrt{2/3}\dot{\gamma}$.

The standard Kuhn–Tucker conditions complete the plasticity description:

$$\dot{\gamma} \geq 0, \qquad \mathcal{F} \leq 0, \qquad \dot{\gamma}\mathcal{F} = 0. \tag{2.31}$$

3. Temperature-dependent parameters

The temperature-dependent parameters of aluminum alloy AW5083, related to both the mechanical and thermal properties are taken from the literature, in particular from [6, 7]. Paper [6] provides values of the density, Young's modulus, heat conductivity, heat capacity, initial yield stress and final yield stress at selected temperatures in the range from room temperature up to 500 °C, denoted by red dots in Fig. 1 to Fig. 6. The temperature on the horizontal axes is given in Kelvins. The blue lines in the figures represent approximations obtained using the least-squares method for the assumed basis functions. In particular, polynomial of a selected degree are used for Young's modulus, density, heat conductivity, and heat capacity, whereas a logistic function is used for the initial and final yield stresses.

The diagram of the thermal expansion coefficient in Fig. 7 is prepared based on the information provided in [7].

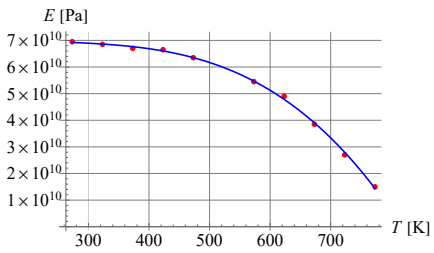

FIG. 1. Young's modulus vs. temperature.

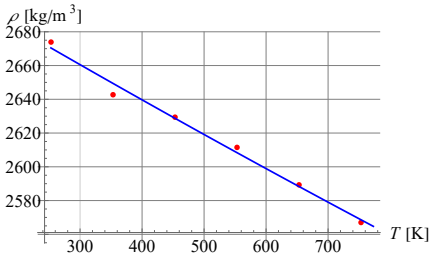

FIG. 2. Density vs. temperature.

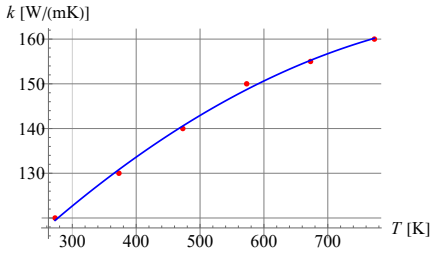

FIG. 3. Heat conductivity vs. temperature.

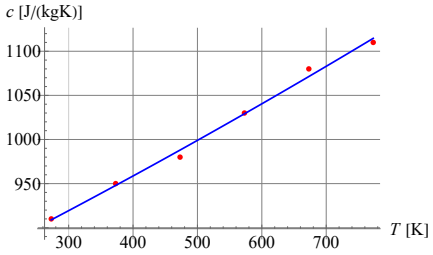

FIG. 4. Heat capacity vs. temperature.

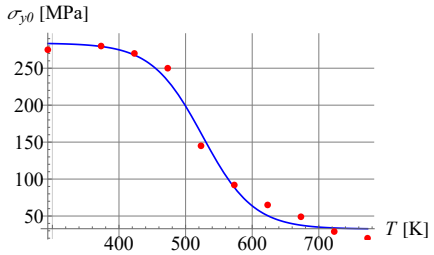

FIG. 5. Initial yield stress vs. temperature.

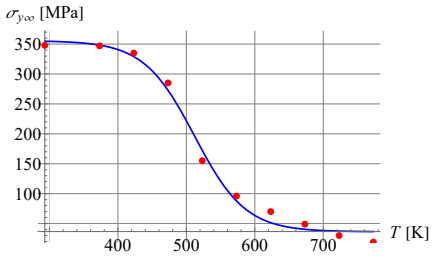

FIG. 6. Ultimate yield stress vs. temperature.

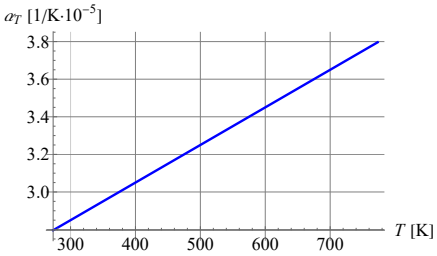

FIG. 7. Thermal expansion coefficient vs. temperature.

The specific formulas describing the temperature-dependent parameters are given in Table 1. The proper values of the parameters are obtained for temperatures given in Kelvins. The resulting units are provided in square brackets.

TABLE 1. Material parameters depending on temperature.

Quantity	Formula
Density [kg/m^3]	$\rho(T) = 2724.97 - 0.219593\,T + 1.58929 \times 10^5\,T^2$
Young's modulus [Pa]	$E(T) = 7.7915 \times 10^{10} - 7.98531 \times 10^7\,T + 273938\,T^2 - 358.197\,T^3$
Thermal expansion coefficient [1/K]	$\alpha_T(T) = 2.25 \times 10^{-5} + 2 \times 10^{-8}\,T$
Heat conductivity [W/(m·K)]	$k(T) = 80.2766 + 0.165482\,T - 8.03571 \times 10^5\,T^2$
Heat capacity [J/(kg·K)]	$c(T) = 807.914 + 0.355393\,T + 5.35714 \times 10^5\,T^2$
Initial yield stress [Pa]	$\sigma_{y0}(T) = 2.83973 \times 10^8 - \dfrac{2.51535 \times 10^8}{1 + \exp(13.769 - 0.0262\,T)}$
Ultimate yield stress [Pa]	$\sigma_{y\infty}(T) = 3.55575 \times 10^8 - \dfrac{3.19238 \times 10^8}{1 + \exp(13.827 - 0.027\,T)}$

It is assumed that Poisson's ratio is constant and equal to $\nu = 0.3$. The bulk and shear moduli present in Eq. (2.21) are calculated on the basis of Young's modulus and Poisson's ratio in the standard way:

$$G(T) = \frac{E(T)}{2[1+\nu]}, \qquad \kappa(T) = \frac{E(T)}{3[1-2\nu]}. \tag{3.1}$$

The value of the saturation parameter is assumed to be equal to $\delta = 19.618$, see [10].

4. NUMERICAL SIMULATIONS

4.1. IMPLEMENTATION

The numerical verification of the presented models of the aluminum alloy AW5083 with the temperature-dependent parameters is performed using the finite element method. The model is implemented within symbolic-numerical packages of Wolfram Mathematica called AceGen/AceFEM, see, e.g., [9]. The finite element (FE) code is developed for 3D hexahedral FEs with the linear interpolation of temperature and displacement fields and the so-called F-bar modification [13], preventing the volumetric locking that occurs in Huber–Mises plasticity. The implementation of large-strain plasticity can be found in [9], whereas the implementation of the coupled thermomechanical model is presented in [14].

Numerical tests include two elongated specimens: one cubic FE in a uniaxial tension state and a dogbone sample which is used commonly for experiments in laboratory, see [10]. For the former sample, the elastic stage is analyzed firstly, followed by the plastic one occurring under greater loading.

Attention is focused on the internal heat sources and their influence on the sample behavior at room temperature and at elevated temperatures up to 500 °C (i.e., 773.15 K).

4.2. Uniaxial tension test

A simulation of a single FE in uniaxial tension is conducted. The cubic specimen has dimensions $L = 10\,\text{mm}$, $W = 10\,\text{mm}$, $H = 10\,\text{mm}$. The visual representation of the FE in 3D space can be seen in Fig. 8. Mechanical boundary conditions are assumed in such a way that uniform deformation is reproduced, and free transverse deformation is allowed. Insulation is applied as thermal boundary conditions.

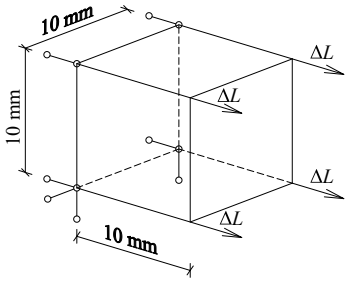

Fig. 8. Visual representation of a single FE in 3D.

4.2.1. Elastic regime analysis

Firstly, the sample is subjected to an enforced elongation of $\Delta L = L/180 = 0.056\,\text{mm}$, applied over a time $t = 10\,\text{s}$. Such elongation allows for the simulation of the sample in the elastic range of as well as the beginning of the plastic deformation phase.

In Fig. 9, the reaction diagrams versus the enforced displacement for different initial temperatures $T_0 = (20,\ 100,\ 200,\ 300,\ 400,\ 500)\,°\text{C}$, are presented. With the increase of the initial temperature, the stiffness of the sample decreases. This phenomenon manifests itself in the graph as a decreasing slope of the gradient. It is shown that the material subjected to elongation enters the plastic range of deformation at different values of ΔL depending on the initial temperature T_0 of the sample, which is an effect of dependence of the initial yield stress on temperature. As the temperature rises, the yield stress decreases. Through the numerical analysis, it is found that the elastic deformation range is the shortest at an initial temperature $T_0 = 400\,°\text{C}$. Although the initial yield stress is lower at temperature 500 °C, the elastic stiffness is significantly smaller and this causes the onset of plasticity to occur later.

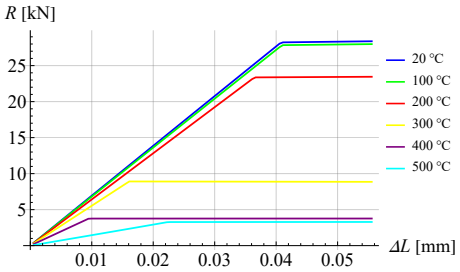

Fig. 9. Sum of reactions vs. enforced displacement for different initial temperatures.

In Fig. 10, the change in the temperature of the sample vs. applied elongation is shown, for the analyzed initial temperatures. In the elastic range of deformations, a decrease in temperature of the sample is seen, and the Gough–Joule effect is observed, which manifests itself as thermo-elastic cooling. An upward tendency of the curves starts at a point at which the behavior of the sample changes, and the material enters the plastic range of deformations. The results of the test presented in Fig. 10 show that depending on the initial temperature the sample enters the state of irreversible deformations at different stages of elongation. It is noted that the biggest thermo-elastic cooling effect is observed at an initial temperature $T_0 = 200\,^{\circ}\mathrm{C}$.

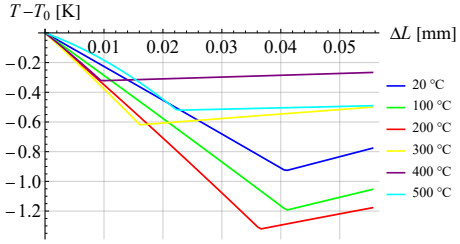

Fig. 10. Relative temperature of the sample vs. enforced displacement for different initial temperatures.

To investigate the influence of the thermo-elastic cooling on the material behavior more thoroughly, Fig. 11 is prepared. It presents the relative temperature at the stage of deformation $\Delta L = 0.0095\,\mathrm{mm}$ for the analyzed initial temperatures. This loading step is the last one at which all tested samples undergo elastic deformation. It can be observed that the strongest effect of the thermo-elastic cooling at the analyzed stage of deformation is for the initial temperature $T_0 = 300\,^{\circ}\mathrm{C}$. As the initial temperature grows from $T_0 = 20\,^{\circ}\mathrm{C}$ up to $T_0 = 300\,^{\circ}\mathrm{C}$ the absolute value of the relative temperature increases gradually. After reaching the $300\,^{\circ}\mathrm{C}$ threshold, the absolute value of relative temperature starts to decrease. This is a result of the value of thermo-elastic cooling source presented in Fig. 12. The observed phenomenon can be explained as follows.

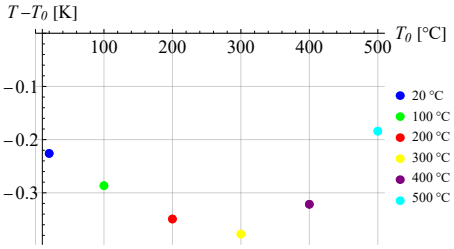

FIG. 11. Relative temperature at $\Delta L = 0.0095\,\text{mm}$ for tests conducted at different initial temperatures.

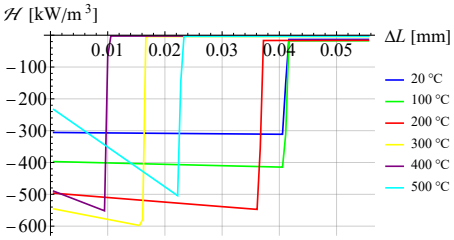

FIG. 12. Elastic cooling for tests conducted at different initial temperatures.

In the analyzed model, the thermo-elastic cooling depends on temperature in two ways, see Eq. (2.18). Firstly, with rising absolute temperature of the sample, the value of the cooling source due to thermo-elastic coupling increases. Secondly, the cooling source also depends on the elastic parameters of the material, especially on Young's modulus which decreases with temperature increase, see Fig. 1. At temperature $623.15\,\text{K} = 350\,^{\circ}\text{C}$, Young's modulus is reduced by almost half. From this moment on, the second effect dominates, leading to a decrease of the source of cooling because of the decreasing stiffness of the material.

4.2.2. Plastic regime analysis

The cubic sample is now subjected to an enforced elongation $\Delta L = L/5 = 2\,\text{mm}$ applied over 1 s, resulting in plastic deformation. Figure 13 and Fig. 14 depict the relationship between the sum of reactions and the enforced displacement for the sample shown in Fig. 8. Both diagrams present the influence of the initial temperature on the mechanical response of the material, but they differ in the type of constitutive model used for testing of the samples. Results obtained for Model 1 are presented in Fig. 13, and for Model 2 in Fig. 14. The graphs capture the transition from elastic to plastic deformation, where the sum of reactions exhibits nonlinear behavior as the displacement increases. Higher initial temperatures typically reduce the yield stress and hardening modulus of aluminum due to thermal softening. This can manifest itself as lower reaction forces for equal displacements for elevated temperatures in Fig. 13 and Fig. 14.

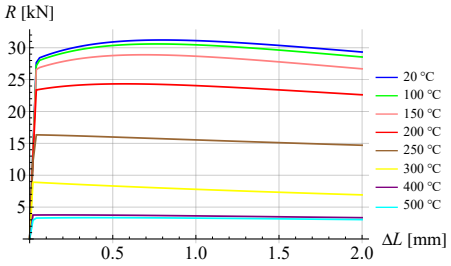

Fig. 13. Sum of reactions vs. enforced displacement at different initial temperatures for Model 1.

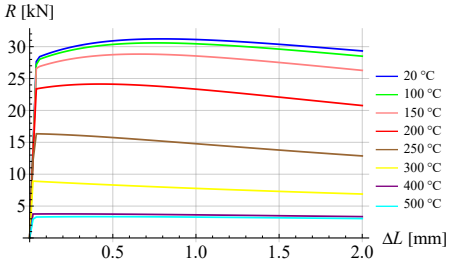

Fig. 14. Sum of reactions vs. enforced displacement at different initial temperatures for Model 2.

Comparing the reactions for Model 1 and Model 2, one can see that a visible difference is present only for two examined reference temperatures: $T_0 = 200\,^\circ\mathrm{C}$ and $T_0 = 250\,^\circ\mathrm{C}$. In comparison with Model 1, Model 2 shows stronger softening of the material at $T_0 = 200\,^\circ\mathrm{C}$. A larger softening can also be observed at $T_0 = 250\,^\circ\mathrm{C}$. After closer examination of the obtained results the differences in reactions at the end of the process between the two models is equal to 8.2 % for $T_0 = 200\,^\circ\mathrm{C}$, and 17.1 ‰ for $T_0 = 500\,^\circ\mathrm{C}$.

Figure 15 and Fig. 16 illustrate the evolution of relative temperature in the aluminum sample subjected to progressive elongation, culminating in plastic deformation. The graphs emphasize the thermomechanical coupling inherent to plastic work and dissipation, with distinct curves representing different initial

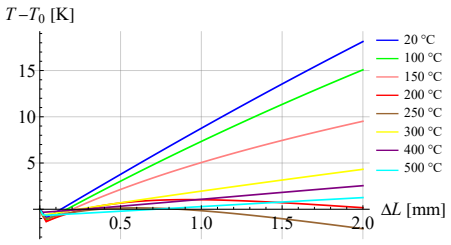

Fig. 15. Relative temperature in the sample vs. enforced displacement at different initial temperatures with Model 1.

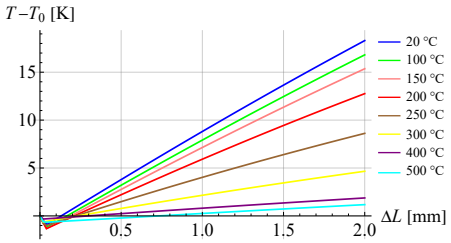

FIG. 16. Relative temperature in the sample vs. enforced displacement at different initial temperatures with Model 2.

temperatures. In the elastic regime, a relative temperature drop is observed, as expected. In the plastic phase of deformation, a pronounced increase in relative temperature occurs due to plastic work conversion to heat. The slope of the diagram of relative temperature vs. displacement increases post-yield, reflecting greater energy dissipation. For higher initial temperatures T_0 the sample exhibits lower values of $T-T_0$ at similar displacements due to lower dissipation. Model 2 reproduces higher heating of the sample compared to Model 1.

Figure 17 and Fig. 18 present the relative temperature $T-T_0$ measured in the aluminum sample at the end of the process, i.e., for the enforced displacement of 2 mm for varying initial temperatures. The graphs compare how temperature evolution differs for various thermomechanical starting conditions. It is clear that

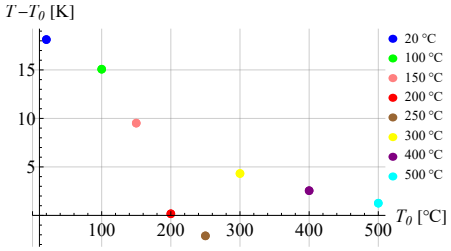

FIG. 17. Relative temperature at $\Delta L = 2$ mm for tests conducted at different initial temperatures for Model 1.

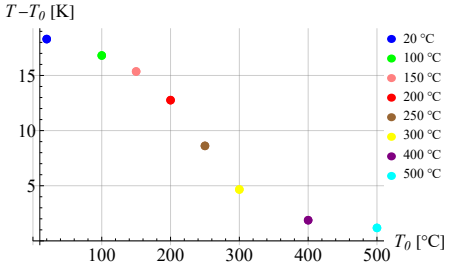

FIG. 18. Relative temperature at $\Delta L = 2$ mm for tests conducted at different initial temperatures for Model 2.

the response of the material differs depending on the type of the computational model applied.

For $T_0 = 20\,^\circ\mathrm{C}$, the difference is hardly noticeable, but at elevated temperatures the sample tested with Model 1 exhibits a smaller raise in relative temperature than samples tested with Model 2. The biggest difference in temperature at the end of the process is observed for $T_0 = 200\,^\circ\mathrm{C}$. For Model 1, the difference is 0.167 K, which means the temperature is almost the same as the reference temperature. For Model 2 it is 20.766 K, which makes for a 20.6 K difference between the two applied models. The analysis presented in Subsec. 4.2.1 shows that at $T_0 = 200\,^\circ\mathrm{C}$, the elastic cooling effect is strong. The heat source associated with plasticity is balanced by the relatively strong Gough–Joule effect, but not exclusively. In Model 1, the heat sources arising from plasticity include not only dissipation, but also the source due to the dependence of material parameters on temperature in the plastic part of the Helmholtz free energy. In such case, this effect manifests itself as heat sinking, which additionally reduces the influence of dissipation. When assuming ψ^p as in Model 2, which is independent of temperature, the sinking effect is absent, which allows for stronger heating of the sample. It is also important that in Model 1 the reduced heating causes smaller thermal softening, which explains why in Fig. 13 the reactions for $T_0 = 200\,^\circ\mathrm{C}$ are much larger in Model 1 than in Model 2. Comparing the graphs from Fig. 17 and Fig. 18, one can notice that Model 2 provides a regular distribution of results over the entire range of analyzed temperatures; therefore, an approximation carried out for the given points decreases monotonously. In turn, in Model 1, with the increase of the initial temperature, the temperature at the end of the process decreases to the point marked in brown, then rises $T_0 = 300\,^\circ\mathrm{C}$. Finally, a downward trend line is observed again.

The quantitative analysis of heating (or sinking) sources for Model 1 can be performed on the basis of Fig. 19 and Fig. 20. The dissipated energy decreases with increasing initial temperature. In contrast, the temperature-hardening coupling causes heat sinking which increases significantly with the growth of the initial temperature up to 200 °C and then decreases, and even exhibits heating

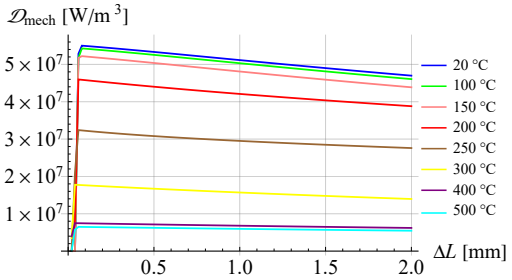

Fig. 19. Dissipated mechanical energy at tests conducted for different initial temperatures for Model 1.

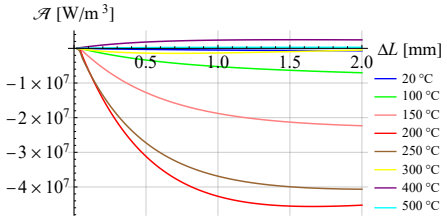

FIG. 20. Heat source related to temperature-hardening coupling for Model 1.

at 400 °C. Note that for $T_0 = 200\,°\mathrm{C}$ in the middle of the process, plastic heating due to energy dissipation is counteracted by heat sinking, cf. red diagrams for $\Delta L = 1\,\mathrm{mm}$ in Fig. 19 and Fig. 20.

4.3. DOGBONE SPECIMEN IN TENSION

To reproduce real experimental testing condition simulations are performed for a dogbone sample geometry described in [10]. The geometry and dimensions of the sample are shown in Fig. 21. The thickness of the specimen is 2 mm. The sample is subjected to maximum elongation of $\Delta L = 30\,\mathrm{mm}$ in time duration of $t_{\max} = 4.95\,\mathrm{s}$.

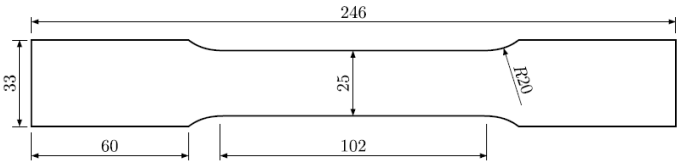

FIG. 21. Dogbone sample – geometry and dimensions (in mm).

4.3.1. TESTS FOR DIFFERENT MESHES

The first set of simulations with Model 1 are performed for three different discretizations. In Fig. 22, one can find visual representation of the three meshes

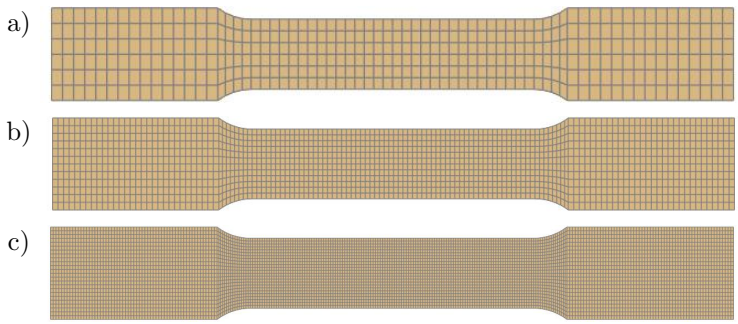

FIG. 22. Visual representation of analyzed meshes: a) coarse, b) medium, c) fine.

used for the tests. The first mesh includes 408 FE, the second 3264, and the third 26 112 elements. In the thickness direction, the coarsest mesh contains one FE, medium mesh two FE, and the finest mesh has four FE. For mesh density analysis, the insulation boundary conditions on all surfaces are assumed and the initial temperature of the sample is the room temperature, i.e., $T_0 = 293.15\,\mathrm{K}$.

The reaction diagram obtained for the analyzed discretizations is presented in Fig. 23. For the thermo-elastic range the results for all three meshes coincide. The same conclusion can be made for the plastic range when material hardens, which takes place until about $\Delta L = 10\,\mathrm{mm}$. After the peak point the decreasing reaction diagrams for different meshes slightly diverge. The descending diagrams are a result of strain localization due to geometrical and thermal softening. Although the results do not coincide, the mesh dependence does not seem to be pathological: the results for the medium and the fine meshes are very close to each other. It is worth mentioning that heat conductivity present in the simulations has a regularizing effect, cf. [15].

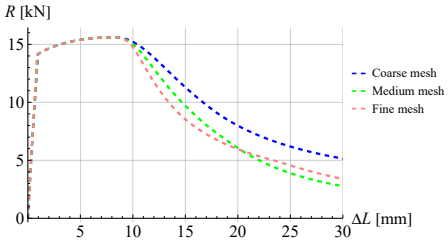

Fig. 23. Reactions depending on the mesh refinement at the midpoint of the sample.

It is observed in Fig. 24 that the temperature in the elastic range and during the hardening phase of plasticity is also the same for all meshes. When localization of deformations occurs, the temperature starts increasing rapidly, because the temperature of the sample is read at the center of the specimen, where plastic deformations are largest. It can also be noticed that the temperature for the medium and fine mesh, starts to decrease at a certain point, but this is not the case for the coarsest mesh. Such phenomenon is an effect of the different forms of localization observed in the considered meshes, presented

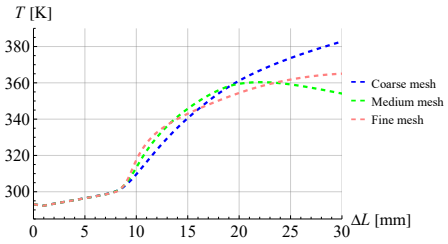

Fig. 24. Temperature depending on the refinement of the mesh at the midpoint of the sample.

in Fig. 25. For the coarse and medium meshes, necking is visible, whereas for the fine mesh, shear bands are present. The finest mesh is chosen for the remaining tests to preserve the accuracy of the obtained results.

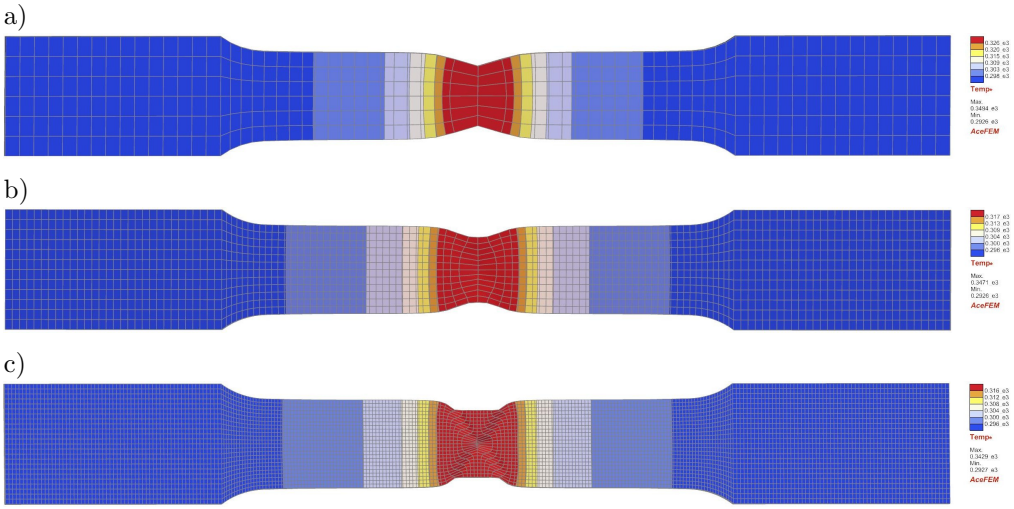

FIG. 25. Deformed meshes with temperature for $\Delta L = 30\,\text{mm}$: a) coarse, b) medium, c) fine.

4.3.2. INFLUENCE OF THERMAL BOUNDARY CONDITIONS

The second set of simulations is performed for Model 1 at room temperature and different thermal boundary conditions, i.e., for insulation and for convection. The heat flux density normal to the specimen surface with convection is defined in the following way:

$$q_n = h_{\text{conv}}(T - T_\infty), \tag{4.1}$$

where T_∞ is the temperature of surrounding and h_{conv} is the convection coefficient. The parameters used in simulations are given in Table 2. A value $h_{\text{conv}} = 0$ corresponds to the insulation boundary condition.

TABLE 2. Convection parameters.

Property	Symbol	Value
Temperature of surrounding [K]	T_∞	T_0
Convection coefficient $[\text{J}/(\text{s}\cdot\text{K}\cdot\text{m}^2)]$	h_{conv}	0, 10, 100

The results shown in Fig. 27 indicate that for all convection coefficients h_{conv} taken into consideration, the temperature response in the range of reversible deformations and in the plastic hardening range coincides. Starting from $\Delta L = 20\,\text{mm}$ the temperature stops increasing, and the slopes of the curves become

increasingly different from each other. Such a phenomenon happens because of the presence of the temperature-hardening coupling in Model 1. With a bigger convection coefficient, greater temperature decrease is observed. Figure 26 shows that the reactions are independent of the chosen convection parameter. For the remaining tests, a convection coefficient $h_{\text{conv}} = 10$ is chosen. For tests performed at elevated temperatures, it is assumed that $T_\infty = T_0$.

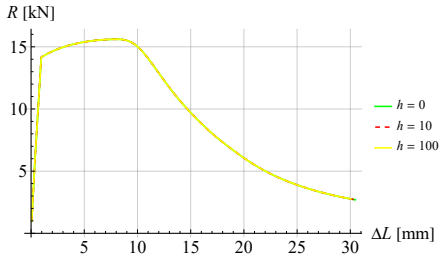

Fig. 26. Reactions independent of the convection coefficient.

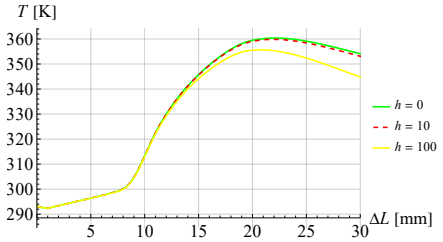

Fig. 27. Temperature difference depending on the value of the convection coefficient h_{conv}.

4.3.3. Model 1 vs. Model 2

The third and core set of simulations includes the tests of sample tension for different initial temperatures. Now, the sample is subjected to an elongation of $\Delta L = L/8 = 30.8\,\text{mm}$ in time duration of $t = 10\,\text{s}$.

Figure 28 and Fig. 29 show the reaction force vs. enforced displacement for Model 1 and Model 2, respectively. For higher initial temperatures, the magni-

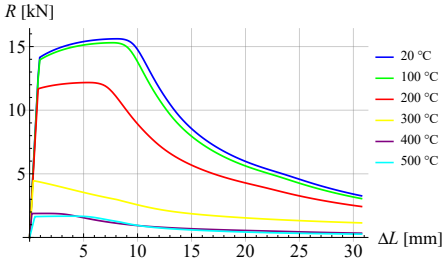

Fig. 28. Sum of reactions vs. enforced displacement at different initial temperatures for Model 1.

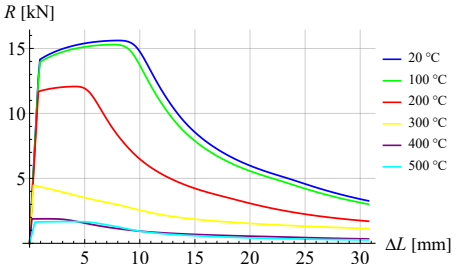

FIG. 29. Sum of reactions vs. enforced displacement at different initial temperatures for Model 2.

tude of reactions decreases, which is consistent with the analysis performed for one FE. The biggest difference between the models is observed for $T_0 = 200\,^{\circ}\mathrm{C}$, similarly to Fig. 14. For Model 2, the material softens earlier than for Model 1. Such behavior is a result of more substantial self-heating in Model 2, causing greater thermal softening.

Figure 30 and Fig. 31 provide a comparison of temperature change versus elongation. Differences between the models are seen for all analyzed temperatures. Model 2 reproduces a bigger temperature rise for lower T_0, but a smaller rise for higher initial temperatures, i.e., $T_0 = 400\,^{\circ}\mathrm{C}$ and $T_0 = 500\,^{\circ}\mathrm{C}$. A significant difference is observed for $T_0 = 200\,^{\circ}\mathrm{C}$, as in this case the amount of

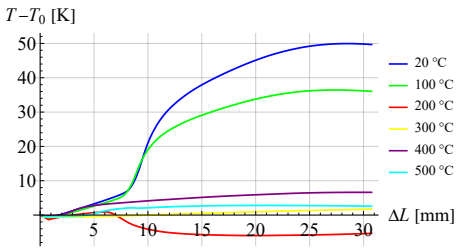

FIG. 30. Relative temperature vs. enforced displacement at different initial temperatures for Model 1.

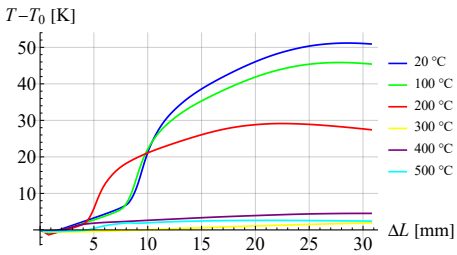

FIG. 31. Relative temperature vs. enforced displacement at different initial temperatures for Model 2.

source sinking due to temperature-hardening coupling exceeds the heat production due to plastic dissipation in the central part of the specimen, where the localization zone occurs. It should also be noted that the results obtained for $T_0 = 300\,^\circ\mathrm{C}$ are not comparable with the remaining results because, in this case, the localization zone is not at the center of the dogbone specimen where the temperature is read, see Fig. 32c. For this reason, the temperature diagram shows a decrease in relative temperature as a result of unloading.

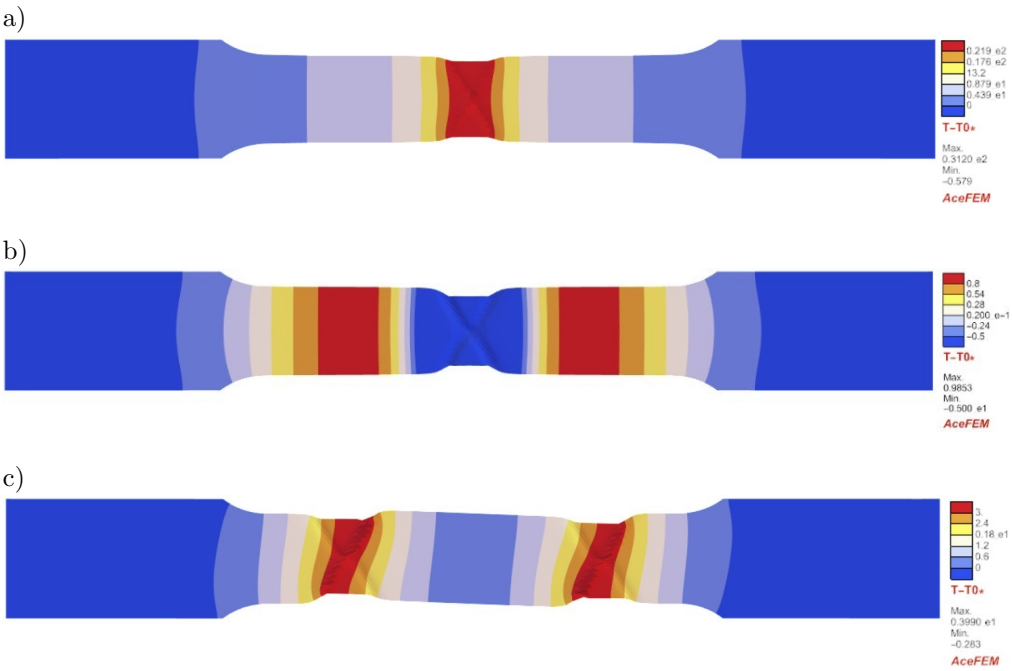

Fig. 32. Deformed mesh with relative temperature at $\Delta L = 12.3\,\mathrm{mm}$ for Model 1: a) $T_0 = 20\,^\circ\mathrm{C}$, b) $T_0 = 200\,^\circ\mathrm{C}$, c) $T_0 = 300\,^\circ\mathrm{C}$.

Figure 32 to Fig. 35 present deformed meshes with temperature and hardening variable distributions for selected initial temperatures, i.e., $20\,^\circ\mathrm{C}$, $200\,^\circ\mathrm{C}$, $300\,^\circ\mathrm{C}$. For $T_0 = 20\,^\circ\mathrm{C}$ and $T_0 = 200\,^\circ\mathrm{C}$, strain localization occurs in the middle part of the sample in the form of two shear bands. As it was mentioned above, the localization for $T_0 = 300\,^\circ\mathrm{C}$ appears in two zones in the web. Only for Model 1 and $T_0 = 200\,^\circ\mathrm{C}$ is the highest temperature not in the shear band areas but outside them. The reason is that thermo-plastic sinking, in this case, is so strong that the area of active plastic process undergoes cooling. Comparing the temperature and hardening variable distributions, it can be observed that the temperature field is more diffused due to heat conductivity.

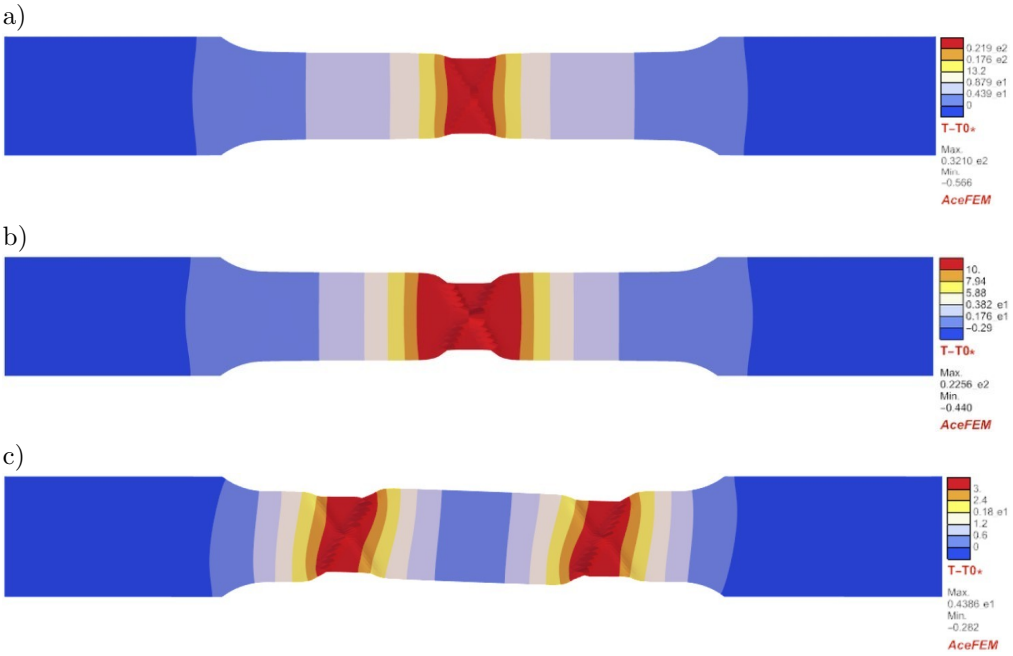

FIG. 33. Deformed mesh with relative temperature at $\Delta L = 12.3\,\text{mm}$ for Model 2: a) $T_0 = 20\,^\circ\text{C}$, b) $T_0 = 200\,^\circ\text{C}$, c) $T_0 = 300\,^\circ\text{C}$.

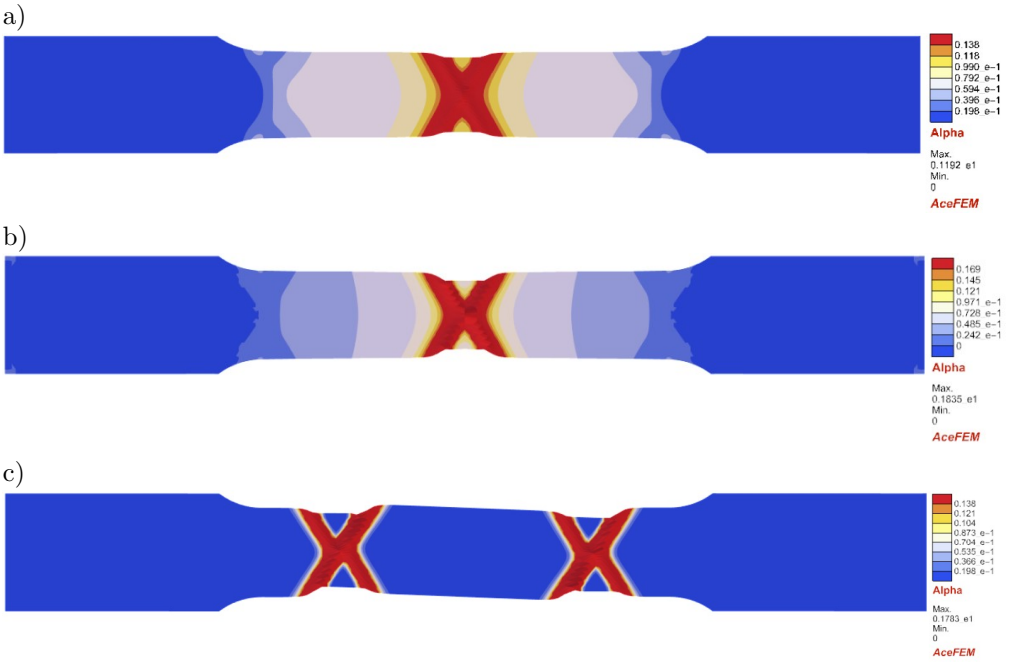

FIG. 34. Deformed mesh with hardening variable at $\Delta L = 12.3\,\text{mm}$ for Model 1: a) $T_0 = 20\,^\circ\text{C}$, b) $T_0 = 200\,^\circ\text{C}$, c) $T_0 = 300\,^\circ\text{C}$.

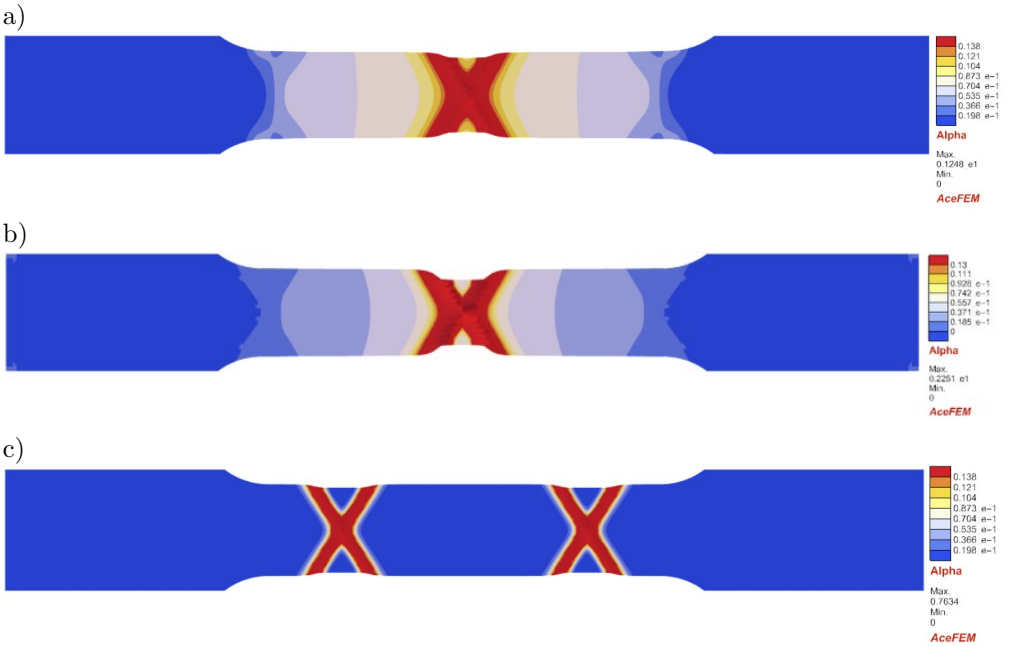

Fig. 35. Deformed mesh with hardening variable at $\Delta L = 12.3\,\text{mm}$ for Model 2: a) $T_0 = 20\,^\circ\text{C}$, b) $T_0 = 200\,^\circ\text{C}$, c) $T_0 = 300\,^\circ\text{C}$.

5. Conclusions

The research presented a comprehensive numerical investigation of aluminum alloy AW5083 under tensile loading, using large-strain thermo-elasto-plastic models. An important aspect of the constitutive description is the application of temperature-dependent material parameters valid in the range from room temperature up to 500 °C together with the employment of internal heat sources. This allowed for numerical simulations of experiments performed at elevated temperatures. The study of the plastic range of deformation was focused on two models of the plastic part of the free energy function. The verification of the influence of temperature-dependent properties on the outcome was performed through simulations of a single cubic FE and dogbone specimens. The models successfully captured fundamental thermo-mechanical phenomena, such as thermo-elastic cooling during elastic deformation and heat generation due to plastic dissipation.

Simulations at different initial temperatures revealed that the Gough–Joule effect is strongest at initial temperature of 300 °C. The elastic modulus, yield stress, and hardening parameters exhibit strong temperature dependence, leading to a reduction of stiffness and earlier yielding at elevated initial temperatures (e.g., 400 °C to 500 °C).

Mesh sensitivity studies show that fine discretization is necessary to reproduce properly the localized deformation modes in the form of shear band(s). Coarser meshes underestimate post-peak softening and misrepresent the localization pattern limiting it to necking. Convection boundary conditions affect the temperature field. Higher convection coefficient accelerate sample cooling and reduce thermal softening.

A thorough comparison between models, including temperature-dependent and temperature-independent plastic free energy, revealed that the largest discrepancies occur between the models at T_0 from 200 °C to 300 °C, where Model 2 predicts stronger material softening due to higher temperature increase. Model 1, including the additional source sinking term resulting from the temperature-hardening coupling, reduces the effect of plastic heating. Moreover, heat sinking for Model 1 is particularly significant in the temperature range from 100 °C to 300 °C and the observed disturbance in this range does not seem consistent with the physics.

Future work should focus on experimental validation in controlled thermal environments to calibrate and refine the models. This would provide crucial data for parameter identification and enhance the models' predictive capabilities. Additionally, extending the framework to include viscous effects, anisotropic behavior, and propagative instabilities such as Portevin–Le Chatelier bands would significantly broaden the model's applicability. Such developments would not only improve the accuracy of the simulations but also contribute to safer and more efficient design of components exposed to extreme thermal and mechanical loads.

Fundings

The work was supported within the Weave-UNISONO program by the German Research Foundation (DFG grant no. 527828607) and by the National Science Centre, Poland (NCN grant no. 2023/05/Y/ST8/00006).

Conflict of interests

The authors declare that there are no known competing financial interests or personal relationships that could have influenced the work described in this paper.

Authors' contributions

Agnieszka Sobierańska carried out the numerical simulations, performed the analysis of the results and wrote the original draft. Balbina Wcisło conceptualized the study, developed the theoretical formulation and implemented the

finite element codes. All authors reviewed literature on the topic, interpreted the results, developed, reviewed, and approved the final manuscript.

Acknowledgement

The authors acknowledge valuable discussions on the research with Prof. Jerzy Pamin and Dr. Marzena Mucha from Cracow University of Technology, Prof. Andreas Menzel from TU Dortmund/Lund University and Dr. Lars Rose from TU Dortmund.

References

1. Simo J.C., Numerical analysis and simulation of plasticity, [in:] *Handbook of Numerical Analysis*, Ciarlet P.G., Lions J.L. [Eds], **6**: 183–499, Elsevier Science B.V., Boca Raton, 1998, https://doi.org/10.1016/S1570-8659(98)80009-4.
2. Ristinmaa M., Wallin M., Ottosen N.S., Thermodynamic format and heat generation of isotropic hardening plasticity, *Acta Mechanica*, **194**: 103–121, 2007, https://doi.org/10.1007/s00707-007-0448-6.
3. Holzapfel G.A., *Nonlinear Solid Mechanics. A Continuum Approach for Engineering*, John Wiley & Sons, Chichester, 2000, https://doi.org/10.1023/A:1020843529530.
4. Oppermann P., Denzer R., Menzel A., A thermo-viscoplasticity model for metals over wide temperature ranges – Application to case hardening steel, *Computational Mechanics*, **69**: 541–563, 2022, https://doi.org/10.1007/s00466-021-02103-4.
5. Ĉanadija M., Brnić J., Associative coupled thermoplasticity at finite strain with temperature-dependent material parameters, *International Journal of Plasticity*, **20**(10): 1851–1874, 2004, https://doi.org/10.1016/j.ijplas.2003.11.016.
6. Summers P.T., Chen Y., Rippe C.M., Allen B., Mouritz A.P., Case S.W., Lattimer B.Y., Overview of aluminum alloy mechanical properties during and after fires, *Fire Science Reviews*, **4**: 3, 2015, https://doi.org/10.1186/s40038-015-0007-5.
7. European Committee for Standardization (CEN), *Eurocode 9 – Design of aluminium structures – Part 1–2: Structural fire design* (Standard no. EN 1991-1-2:2023), p. 16, 2023.
8. Wcisło B., Mucha M., Pamin J., Internal heat sources in large strain thermo-elasto-plasticity – Theory and finite element simulations, *Journal of Theoretical and Applied Mechanics*, **62**(2): 293–306, 2024, https://doi.org/10.15632/jtam-pl/185614.
9. Korelc J., Wriggers P., *Automation of Finite Element Methods*, Springer, Cham, 2016, https://doi.org/10.1007/978-3-319-39005-5.
10. Mucha M., Rose L., Wcisło B., Menzel A., Pamin J., Experiments and numerical simulations of Lueders bands and Portevin–Le Chatelier effect in aluminium alloy AW5083, *Archives of Mechanics*, **75**(3): 301–336, 2023, https://doi.org/10.24423/aom.4204.
11. Miehe C., Entropic thermoelasticity at finite strains. Aspects of the formulation and numerical implementation, *Computer Methods in Applied Mechanics and Engineering*, **120**(3–4): 243–269, 1995, https://doi.org/10.1016/0045-7825(94)00057-T.

12. Wcisło B., Pamin J., Rose L., Menzel A., On spatial vs referential isotropic Fourier's law in finite deformation thermomechanics, *Engineering Transactions*, **71**(1): 111–140, 2023, https://doi.org/10.24423/EngTrans.2460.20230214.

13. de Souza Neto E.A., Perić D., Owen D.R.J., *Computational Methods for Plasticity: Theory and Applications*, John Wiley & Sons, Chichester, 2008, https://doi.org/10.1002/9780470694626.

14. Wcisło B., Pamin J., Local and non-local thermomechanical modeling of elastic-plastic materials undergoing large strains, *International Journal for Numerical Methods in Engineering*, **109**(1): 102–124, 2017, https://doi.org/10.1002/nme.5280.

15. Lemonds J., Needleman A., Finite element analyses of shear localization in rate and temperature dependent solids, *Mechanics of Materials*, **5**(4): 339–361, 1986, https://doi.org/10.1016/0167-6636(86)90039-6.

Received August 13, 2025; revised October 26, 2025; accepted October 30, 2025; available online December 18, 2025; version of record April 16, 2026; published issue June 24, 2026.